THE ASTROPHYSICAL JOURNAL, 432:L59–L62, 1994 September 1

WIDESPREAD WATER VAPOR EMISSION IN ORION

J. CERNICHARO,[1] E. GONZÁLEZ-ALFONSO,[1,2] J. ALCOLEA,[1] R. BACHILLER,[1] AND D. JOHN[3]
Received 1994 March 7; accepted 1994 June 7

ABSTRACT

We have discovered spatially extended emission in the 3_{13}–2_{20} line of water vapor in Orion. This is the first time that extended water emission has been found in the interstellar medium. Many strong narrow features with flux density $\sim(1\text{–}15) \times 10^3$ Jy have been detected around Ori A–IRc2. These features appear superposed over a weaker ($\sim 10^3$ Jy) high velocity plateau with a half-power size of $\approx 45''$, and a total extent of $80'' \times 80''$. Narrow lines with intensities $\sim$25–200 Jy, are detected at the velocity of the molecular cloud for all the positions observed along the molecular ridge. These lines are not arising from point sources and the different emission regions are well resolved by our 15″ beam. Narrow and blueshifted emission is also found along a filament containing the S6 source 100″ south of IRc2. From statistical equilibrium and radiative transfer calculations for the physical conditions of the Orion molecular cloud, we conclude that the nature of the observed water vapor emission is dominated by maser emission. The water abundance is estimated to be larger than 10^{-5}, implying that water vapor is a substantial component of the gas phase in warm molecular clouds and one of its most important gas coolants.

Subject headings: ISM: abundances — ISM: clouds — ISM: individual (Orion IRc2) — ISM: jets and outflows — ISM: molecules

1. INTRODUCTION

Water vapor, one of the first molecules observed in radio astronomy, was discovered in 1969 by Cheung et al. through the maser emission of its 6_{16}–5_{23} rotational transition at 22 GHz. Since then, many lines of water have been observed at submillimeter wavelengths from the ground (Menten et al. 1990a, b; Menten & Melnick 1991; Cernicharo et al. 1990 [hereafter Paper I], 1994). However, all the water lines detected so far are likely to be masing, and probably arise from pointlike sources. Because water vapor is predicted to be an abundant molecule in the gas phase, a determination of its spatial extent and distribution is crucial in modeling the chemistry and the physics of warm molecular clouds. In Paper I we reported observations of the 3_{13}–2_{20} rotational transition of para-water at 183.3 GHz which lies only 200 K above the ground level. This line was detected at several positions in Ori A–IRc2, and consists of a broad plateau with many strong and narrow features arising from two different directions separated by 20″. Evidence for both narrow and weak emission was found 100″ away of IRc2, but the resulting maps were spatially limited precluding any detailed analysis of para-water emission in this cloud. In this *Letter* we report the observation of water emission over a region around Ori A–IRc2 of $160'' \times 240''$.

2. OBSERVATIONS

The new observations of the 3_{13}–2_{20} line of para-water vapor at 183.310 GHz were carried out on 1994 January 17 with the IRAM 30 m radio telescope (see also Paper I). These were taken under excellent weather conditions, with temperatures of $-15°$ C, and very low relative humidity. Measured zenith opacities at the center of the telluric water line were $\approx$0.6–0.7, which correspond to a water vapor amounts above the telescope site of 0.25–0.3 mm (Cernicharo 1985). The atmospheric transmission was so good that mesopheric water emission was easily detected, which is an indication of the transparency of the low altitude terrestrial atmosphere (Cernicharo et al. 1994). Due to these excellent weather conditions, the uncertainty on the calibration of the present observations is below 30%.

During the 1994 observations, we used three SIS receivers in parallel. The 2 mm receiver was tuned in DSB with a receiver temperature of 250 K. The water line was in the USB, with SSB system temperatures of $\sim$2000–4000 K. The 3 mm receiver was tuned at the frequency of the $v = 1$ $J = 2$–1 line of SiO to point the telescope on IRc2 itself. The 230 GHz receiver was tuned at the CO $J = 2$–1 frequency in order to compare the CO and H_2O spatial distributions. SSB receiver and system temperatures were 140 and 220 K, respectively. The three receivers were aligned within 2″. Pointing was monitored every 20 minutes. The velocity resolution at 183.3 GHz was 1.6 km s^{-1} with the 1 MHz filters (bandwidth of 812 km s^{-1}) and 0.12 km s^{-1} with the autocorrelator (bandwidth of 120 km s^{-1}). At 183.3 GHz the main beam efficiency of the telescope is 0.55 and its half-power beamwidth is 15″. The observing procedure consisted in several rasters in declination (for different right ascension offsets) with 3 ONs per OFF. Calibration was performed at the beginning of each raster observation, and the center position (IRc2) was observed every two rasters. No changes in the intensity larger than 10% were observed. The map spacing was 10″ in the central region ($120'' \times 120''$), and 20″ outside.

In order to analyze the shape of the main and secondary beams at 183.3 GHz when convolved with an extended source, we observed Jupiter in continuum mode over several azimuth-elevation scans (at the same parallactic angle than the observations of the Orion central region). Comparing the water emission far away of IRc2 with the Jupiter scans, we conclude that the normalized (to the maximum intensity) water intensity at $\Delta\delta = -100''$ was 15 times stronger than that observed in the Jupiter. At $\Delta\delta = 120''$, it was 6 times larger. Consequently, the large extent of the water emission in Orion is not produced by

[1] Centro Astronómico de Yebes, Apartado 148, E-19080 Guadalajara, Spain.
[2] Universidad de Alcala de Henares, Departamento de Física, Campus Universitario, E-28871 Alcala de Henares, Spain.
[3] IRAM, Av. Divina Pastora N7 NC, E-18012 Granada, Spain.

contamination of the central source in the secondary beams of the telescope.

3. RESULTS

Figure 1*a* shows the observed spectra in the central region around IRc2 (30″ × 30″); Figure 1*b* shows the water spectra over a larger region but a different scale illustrating the large spatial extent of the water emission. Figure 2 displays the spectra observed along a declination strip through $\Delta\alpha = 0''$. False color maps of the water integrated intensity for different velocity intervals are shown in Figure 3 (Plate L3), which also includes for comparison purposes the corresponding contour maps for the CO $J = 2$–1 emission. The water emission in Orion consists of many narrow and strong features concentrated in a region of 30″ × 30″ around Ori A–IRc2 which are superposed on a high-velocity velocity plateau extending over a velocity range of ± 100 km s^{-1} (see Fig. 1*b*). The high-velocity plateau is seen as far as 40″ from IRc2. Farther out, the water emission becomes weaker ($T_A^* = 5$–40 K) and is only seen at the ambient velocities.

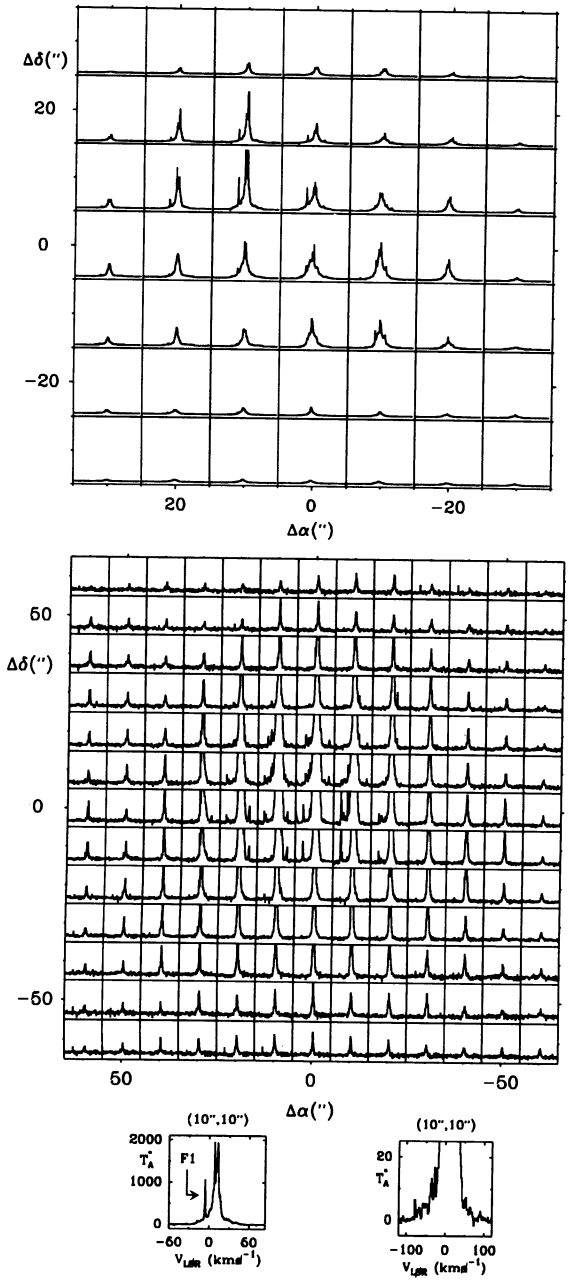

FIG. 1.—Observed spectra around IRc2 over a region 60″ × 60″ wide (*a*) and 120″ × 120″ wide. (*b*) The LSR velocity range and antenna temperature limits are −50 to 70 km s^{-1} and −100 to 2100 K for (*a*) (as indicated in the left bottom box), and −120 to 120 km s^{-1}, and −5 to 25 K for (*b*) (as indicated in the right bottom box). Position offsets are given with respect to IRc2 ($\alpha_{1950} = 5^h32^m47^s$, $\delta_{1950} = -5°24'23''.6$).

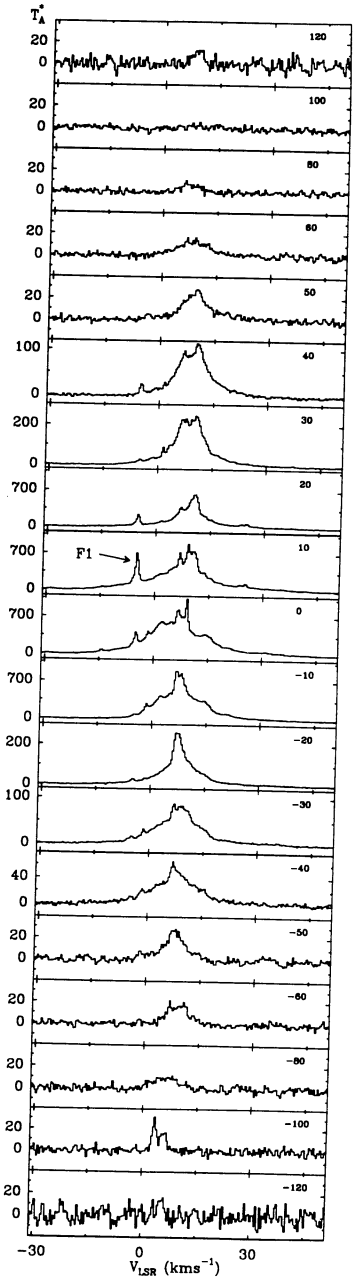

FIG. 2.—Observed spectra along a declination strip for $\Delta\alpha = 0$. The declination offset is indicated at the top-right corner of each panel. Note the velocity changes near the S6 source at $\Delta\delta = -100''$.

3.1. *Narrow Features*

The narrow and low-velocity features of Figures 1 and 2 are spatially distributed in two different regions northeast and

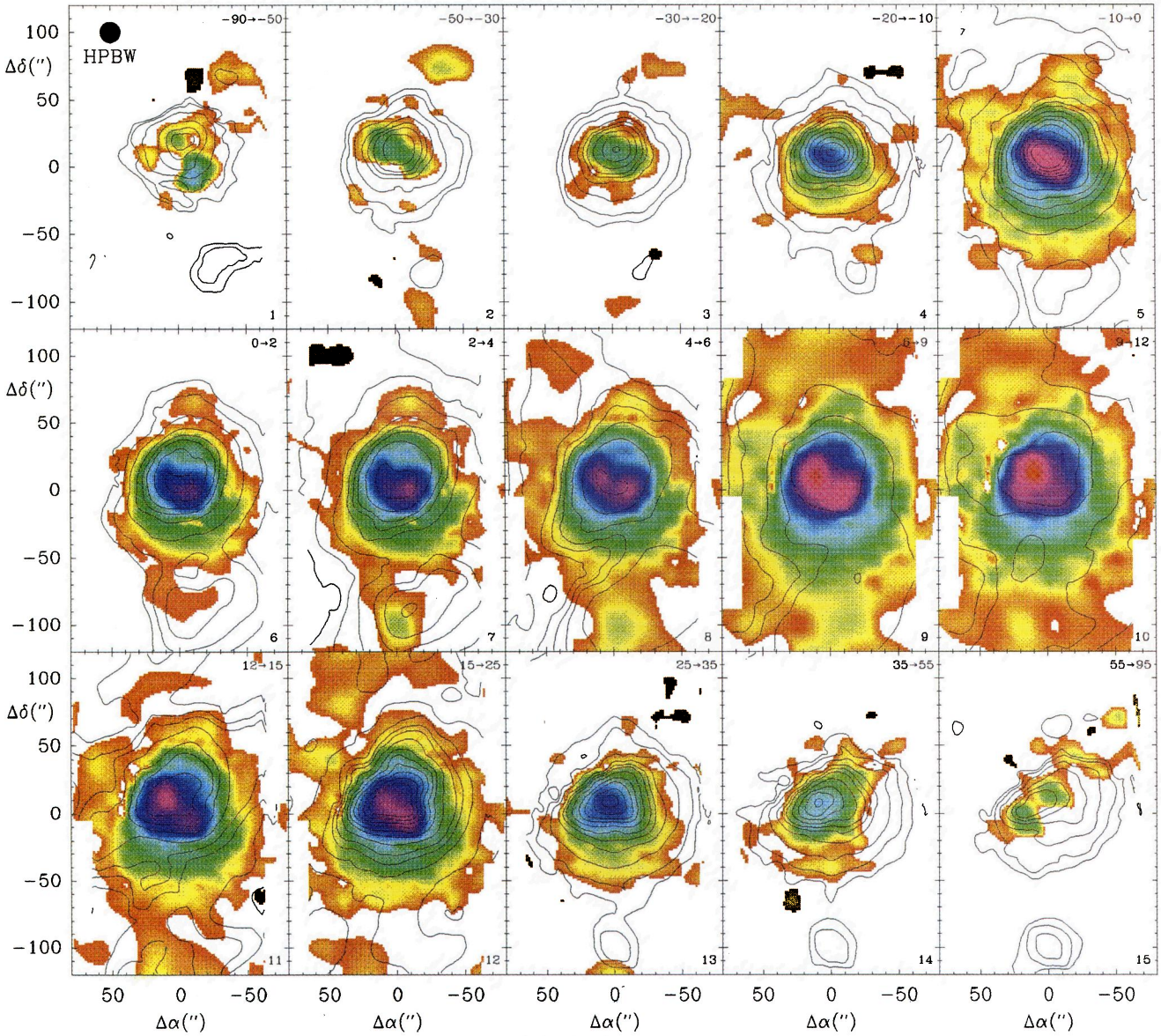

FIG. 3.—Water emission integrated intensity color maps for different velocity ranges. The black contours correspond to the CO emission in the same velocity intervals. The CO data were observed simultaneously with the water emission. They are shown here for comparison purposes and will be analyzed in detail elsewhere (Rodriguez-Franco et al. 1994). The panels are labeled at their bottom-right corners, and the corresponding velocity intervals in km s^{-1} are given at their top-right corners. Note the different filaments arising at different velocities and in particular the one appearing at 2 km s^{-1} and running from east of IRc2 to S6. The first color contour corresponds to 7.5 K km s^{-1} and the strongest value to 4200 K km s^{-1}. The water emission maxima in maps 1–15 are 200, 113, 110, 483, 2386, 1043, 1382, 1574, 3312, 4180, 1857, 1537, 583, 214, and 89 K km s^{-1}, respectively. The CO contours are 3, 5, 10, 20, 30, 40, 60, 90, 120, 160, 200, 250, and 300 K km s^{-1}. For clarity, some CO low contours are not displayed in the panels 8–12; the first CO contours in these panels are 5, 40, 80, 10, and 5 K km s^{-1}, respectively.

southwest of IRc2 which correspond to the region where the low-velocity 22 GHz maser spots are observed (see Fig. 2 of Paper I and Figs. 1 and 3 of this paper). The line width of these features is 1–3 km s^{-1} at half-intensity. A comparison of Figure 1 in Paper I with the data shown in Figure 1 of this paper indicates that some of these features have strong flux variations, confirming their maser nature. Intensity and line shape variations for this transition of para-water have been also reported by Kuiper et al. (1984) from their observations with the KAO. Weak high-velocity ($|v| > 30$ km s^{-1}) features which were detected in both observing periods do not present significant changes in velocity or intensity. Although the strongest high-velocity features are concentrated around IRc2, some of them are seen far away from this source. For instance, a 75 Jy feature at 37 km s^{-1} is detected at (−20″, 30″) (Fig. 1*b*).

One of the most remarkable low-velocity features is that at −4.9 km s^{-1} (labeled F1 in Figs. 1*a* and 2), which was quite weak in the 1989 data but very strong in 1994. A map produced by removing the neighboring emission to F1 gives for this feature a deconvolved size at half-power of $13(\pm 1.6)'' \times 7(\pm 3)''$; i.e., it appears as marginally extended. These flux variations can be related to variations of the water column density and/or of the kinetic gas temperature. In the unsaturated masing regime, relative small variations in T_K may lead to high variations in T_B provided that the water column density is high enough ($\approx 6 \times 10^{17}$ cm^{-2}), and T_K is ≈60–100 K. Large velocity gradient (LVG) calculations (see below for details) show that for $T_K = 100$ K and $n(H_2) = 10^5$ cm^{-3}, variations of $\Delta T_K = 30$ K induce variations in T_B of almost one order of magnitude.

3.2. *Broad High-Velocity Emission*

The broad velocity emission plateau is the most conspicuous feature of the water emission in Orion. It is clearly spatially extended, and covers a velocity range ±100 km s^{-1} (see Fig. 3) similar to the CO wings. After removing the narrow features, its intensity reaches 300–500 K at the peak. Figure 3 shows the spatial distribution of the wings at different velocities (see also Figs. 1 and 2). At velocities −90 to −50 km s^{-1} (Fig. 3, panel 1) water emission arises from two different regions. One of them is shifted by 20″ south of the CO peak, and the other is shifted 10″ east. Weak emission is found 20″ south of the HH objects HH 5, 6, and 7 (Jones & Walker 1986), where CO only presents marginal emission. Water emission probably arises at the shocked regions associated to the HH objects. This region peaks at velocities between −50 and −30 km s^{-1} at the position (−35″, +75″) (see panel 2 of Fig. 3). At extreme positive velocities (between 55 and 95 km s^{-1}; see panel 15) the water emission has an elongated distribution following closely the northern edge of the CO emission. Both the highest blue and redshifted velocities of the water emission (panels 1 and 15) consist of a chain of emission peaks extending over 1′ and coexisting spatially. The position centroids of these components are located 10″–15″ N from IRc2 (see Figs. 1 and 2), similar to the high-velocity CO emission (Wilson, Serabyn, & Henkel 1986). For the other large velocities the water emission is embedded in the CO emission region (panels 3, 4, 13, and 14 of Fig. 3). For low red and blue velocities the total extent of the water emission is larger than 80″ (panels 5 and 12). In panel 5 a narrow filament appears at velocities between −10 and 0 km s^{-1} around (50″, 40″), which agrees in position with the filament detected in the emission of dust grains at 3.3 μm by Gatley & Kaifu (1987). The water emission from this filament peaks at ambient velocities and presents moderate velocity wings. This filament, together with one arising at (70″, −100″) (panel 9), delineate a curved structure similar to that found at 3.3 μm, which probably arises from the interaction of the H II region with the molecular cloud.

3.3. *The Molecular Ridge*

Central velocities in Figure 3 (panels 6–11) show an intricate behavior for the water emission. In addition to the features around IRc2, a narrow filament is found toward the south. It is apparent at velocities 0 to 2 km s^{-1} (panel 6) and becomes particularly strong in the velocity range 4 to 8 km s^{-1} (panels 8 and 9). It shows a strong velocity gradient from north to south, and an important shift in position from east to west. The water filament agrees in position with the molecular ridge (see, e.g., the HC_3N maps of Rodríguez-Franco et al., 1992) but its velocity is blueshifted by 2–3 km s^{-1} (see Fig. 2). It appears spatially broader than CO and at the east limit of the CO molecular ridge in panels 6 and 7. The water emission along this filament peaks on the S6 source (Bartla et al. 1983; Schmid-Burgk et al. 1990), where it consists of two velocity components at 3.3 and 6 km s^{-1} (see Fig. 2). As the velocity increases, the emission moves toward the west until the velocity reaches 6–9 km s^{-1}, and then begins to move again toward the east (panels 10 and 11). This velocity and spatial structure suggest an envelope surrounding the molecular ridge and perturbed by an ionization-shock front propagating into the neutral gas. At the north of IRc2, moderate emission is found at ambient velocities (9 km s^{-1}) following the shape of the CO emission. The line profiles present weak red wings from 15 to 25 km s^{-1} along a filament arising at the NE of IRc2 and running clockwise toward the NW (see panel 12 of Fig. 3; the filament is also apparent in panels 9, 10, and 11). The blueshifted counterpart is weak, remaining undetected at most positions.

4. DISCUSSION

We have modeled the radiative transfer of the rotational levels of *p*–H_2O under a escape probability formalism for the physical conditions characterizing the molecular ridge ($T_K \approx$ 60 K, $n(H_2) = 10^5$–10^6 cm^{-3} and $N(H_2) = 10^{22}$–10^{23} cm^{-2}, see, e.g., Rodriguez-Franco et al. 1992). The model consists of a spherical turbulent cloud with no velocity gradient, in which all the physical parameters are assumed to be uniform. Mean escape probabilities for nonmasing transitions were taken from Capriotti (1965), and those for masing transitions were computed numerically by assuming an absorption Doppler profile. Collisional rates between water and helium were taken from Green, Maluendes, & McLean (1993). Helium abundance was assumed to be 0.1, and the rates were corrected to take into account the collisions between water and molecular hydrogen. We calculated the statistical equilibrium populations of the lowest 15 rotational levels for $T_K = 60$ K, and a microturbulent velocity of 2 km s^{-1}. Under these conditions, only the 183 GHz transition was found to be inverted with appreciable amplification. We also modeled the low-velocity plateau emission as a spherical cloud at $T_K = 150$ K. In this case, we used the LVG code to simulate the observed large velocity dispersion (≈30 km s^{-1}), including the lowest 17 rotational levels.

Figure 4 shows the brightest temperature T_B and the radial opacity of the 183 GHz line toward the center of the cloud versus the *p*–H_2O column density for different H_2 volume densities for the ridge (Fig. 4*a*), and the plateau (Fig. 4*b*). For the ridge, a maser effect is found for $N(p\text{–}H_2O) < 7 \times 10^{18}$ cm^{-2} and $n(H_2) = 10^5$–10^6 cm^{-3}. For higher column densities, the decay rates from the masing levels decrease, and the maser is

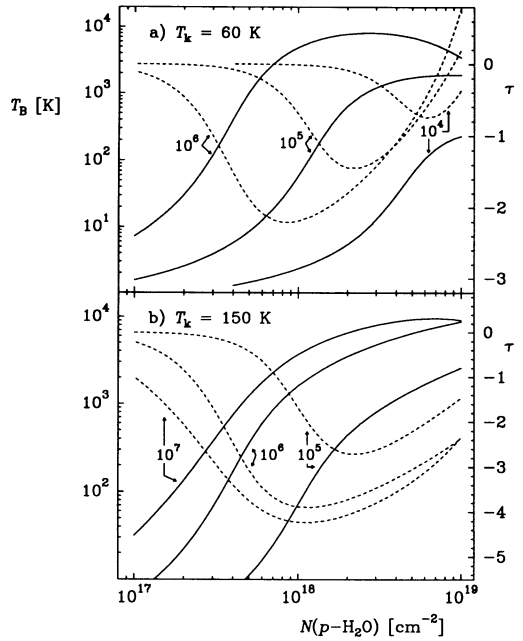

FIG. 4.—(*a–b*) Results from statistical equilibrium calculations for the 3_{13}–2_{20} line of para-water for different densities and temperatures (see text). Solid lines represent brightness temperatures, while dashed lines represent opacity. The gas density (in cm^{-3}) is indicated for each curve.

quenched due to spontaneous radiative decay. However, the ratio of the pump rate to the decay rate of the upper level, R_u, remains still higher than for the lower level, and the excitation temperature of the transition is suprathermal ($T_B > T_K$). In the 10^5 cm^{-3} curve, T_B still increases when the inversion disappear because R_u-R_l increases with water column density. Figure 4*a* shows that even at $T_K = 60$ K, T_B is high enough to explain the observed extended emission for moderate values of $n(H_2)$ and $N(p\text{-}H_2O)$. For instance, a density of $n(H_2) = 10^5$ cm^{-3}, together with $N(p\text{-}H_2O) \geq 6 \times 10^{17}$ cm^{-2}, leads to T_B values larger than 10 K, a typical value of the brightness temperature for the molecular ridge. Assuming an [ortho]/[para] ratio of 3 and a column density of molecular hydrogen between 10^{22} and 10^{23} cm^{-2}, the corresponding water abundance is $\approx 10^{-4}$–2×10^{-5}. The observed brightness temperature of the widespread emission is well above 1 K, which imposes a firm lower limit of 10^{-5} to the water abundance in the Orion molecular ridge (for an assumed density of 10^5 cm^{-3}). This lower limit is at least three orders of magnitude larger than the upper limits derived by Wannier et al. (1991) from observations of the 1_{10}–1_{01} line of $H_2{}^{18}O$. However, our estimate for the column density of water agrees reasonably well with the value derived by Jacq et al. (1988) from the 3_{13}–2_{20} line of $H_2{}^{18}O$ and with those derived from HDO (see, e.g., Olofsson 1984). The only way to reproduce the observed intensities with a lower water abundance in the molecular ridge is to increase the kinetic temperature from 60 to 200–300 K. However, there are not indications for such a high temperature on spatial scales as large as those revealed by our data. For the plateau, the transition is inverted over the whole range of $N(p\text{-}H_2O)$, and the maser begins to saturate for $N(p\text{-}H_2O) > 10^{18}$ cm^{-2} (see Fig. 4*b*). The observed plateau emission (T_B = a few 10^2 K) is well explained with values for $N(p\text{-}H_2O)$ comparable to those found in the ridge. For a density of 10^6 cm^{-3} and a kinetic temperature of 150 K we derive a para-water column density of 6×10^{17}–10^{18} cm^{-2}. The CO column density in the plateau derived from our $J = 2$–1 data, and for the same physical parameters, is $\approx 8 \times 10^{18}$ cm^{-2}. Hence, the H_2O/CO abundance ratio is 0.3–0.5.

The high water abundances derived in this paper confirm, as has been long suspected (see, e.g., the recent paper by Neufeld & Kaufman 1993 and references therein), that water is the dominant gas coolant in warm molecular clouds through its emission at submillimeter and infrared wavelengths. The relatively low temperatures and moderate densities required for the line inversion, together with the strong dependence of the emission upon the kinetic temperature, makes the water 183 GHz line an excellent tracer of hot/shocked gas in molecular clouds.

We thank A. Rodríguez-Franco, J. Martín-Pintado, M. Guélin, P. Cox, M. Elitzur, V. Bujarrabal, and C. M. Walmsley for useful comments and suggestions. This work was partially supported by Spanish DGICYT under project PB90-408.

REFERENCES

Bartla, W., Wilson, T. L., Bastien, P., & Ruf, K. 1983, A&A, 128, 279
Capriotti, E. R. 1965, ApJ, 142, 1101
Cernicharo, J. 1985, IRAM internal report
Cernicharo, J., Thum, C., Hein, H., John D., Garcia, P., & Mattioco, F. 1990, A&A, 231, L15 (Paper I)
Cernicharo, J., González-Alfonso, E., & Alcolea, J. 1994, A&A, submitted
Cheung, A. C., Rank, D. M., Townes, C. H., Thornton, D. D., & Welch, W. J. 1969, Nature, 221, 626
Gatley, I., & Kaifu, N. 1987, in Astrochemistry, ed. M. S. Vardya & S. P. Tarafdar (Dordrecht: Reidel), 153
Green, S., Maluendes, S., & McLean, A. D. 1993, ApJS, 85, 181
Jacq, T., Jewell, P. R., Henkel, C., Walmsley, C. M., Baudry, A. 1988, A&A, 199, L5
Jones, B. F., & Walker, M. F. 1985, AJ, 90, 1320
Kuiper, T. B. H., Rodriguez Kuiper, E. N., Swanson, P. N., Dickinson, D. F., Kein, M. J., & Zimmermann, P. 1984, ApJ, 283, 106
Menten, K., & Melnick, G. J. 1991, ApJ, 377, 647
Menten, K., Melnick, G. J., & Phillips, T. G. 1990a, ApJ, 350, L41
Menten, K., Melnick, G. J., Phillips, T. G., & Neufeld, D. A. 1990b, ApJ, 350, L27
Neufeld, D. A., & Kaufman, M. J. 1993, ApJ, 418, 263
Olofsson, H. 1984, A&A, 134, 36
Rodriguez-Franco, A., Martín-Pintado, J., Gómez-González, J., & Planesas, P. 1992, A&A, 264, 592
Schmid-Burgk, J., Güsten, R., Mauersberger, R., Schulz, A., & Wilson, T. L. 1990, ApJ, 362, L25
Wannier, P. G., et al. 1991, ApJ, 377, 171
Wilson, T. L., Serabyn, E., & Henkel, C. 1986, A&A, 167, L17